ADVANCED FUNCTIONAL MATERIALS
www.afm-journal.de

Photocurrent-Directed Immunoregulation Accelerates Osseointegration through Activating Calcium Influx in Macrophages

Yizhou Zhu, Chaofeng Wang, Can Ai, Yiming Xiang, Congyang Mao, Wei Qiao, Jun Wu, John Akrofi Kubi, Xiangmei Liu, Shuilin Wu,* Xin Zhao, Bin Li, and Kelvin W. K. Yeung**

Early osteoimmune microenvironment disorder at the interface between bone and implant can lead to implant loosening, which prolongs patient convalescence, exacerbates postoperative complications, and potentially results in implant failure. The timely regulation of macrophages primarily orchestrates the entire long-term regeneration process. Here, it is proposed to precisely direct macrophage polarization using localized photoelectrical signals generated by an excitable surface in response to remote stimulation via near-infrared light (NIR). The photocurrent generated from the n–n heterojunction between calcium titanate ($CaTiO_3$) and defective titanium dioxide (TiO_2-V_o) on the excitable surface can accurately direct macrophage polarization, suppressing acute inflammation at the early stage of post-implantation and establishing a favorable osteoimmune microenvironment that promotes bone-to-implant integration. Mechanistic study reveals that photoelectric signals initiate increased calcium influx via voltage-gated calcium ion channels, subsequently modulating calcium/calmodulin-dependent protein kinase kinase 2 (Camkk2) and calcium/calmodulin-dependent protein kinase I (Camk1) expression to regulate macrophage polarization. This optimization of the osteoimmune microenvironment results in enhanced mesenchymal stem cells (MSCs) recruitment and osteogenesis, ultimately accelerating bone-to-implant integration within 14 days post-implantation. This research presents a novel method for adjusting in vivo spatiotemporal immune responses through the use of noninvasive and externally-controlled targeted stimulations.

1. Introduction

Foreign body reaction (FBR) is an inevitable physiological response that occurs upon the introduction of implants into the body.[1] This complex process encompasses a series of cellular and molecular events, which ultimately determine the outcome of implant integration.[2] Macrophages, as one of the earliest arriving immune cells, play the central role in FBR and mediate subsequent cascades throughout the entire biological process of bone-to-implant integration.[3] Upon implantation, macrophages initiate an acute inflammation response by producing soluble mediators, such as cytokines like transient tumor necrosis factor-alpha (TNF-α), to facilitate the recruitment of mesenchymal stem cells (MSCs) and initiate the regenerative process.[4] This essential proinflammatory process begins immediately upon implantation and peaks within 24–48 h.[5] However, in cases where the host immune system's self-regulation is compromised due to the local pathological conditions, the spike in inflammation may not be adjusted in time and progress into chronic inflammation.[6] This

Y. Zhu, C. Ai, Y. Xiang, C. Mao, W. Qiao, J. Wu, J. A. Kubi, K. W. K. Yeung
Department of Orthopaedics & Traumatology
Li Ka Shing Faculty of Medicine
The University of Hong Kong
Pokfulam, Hong Kong 999077, China
E-mail: wkkyeung@hku.hk

Y. Zhu, C. Wang, Y. Xiang, C. Mao, X. Liu, S. Wu
Biomedical Materials Engineering Research Center
Collaborative Innovation Center for Advanced Organic Chemical Materials Co-Constructed by the Province and Ministry
Hubei University
Wuhan 430062, China
E-mail: liuxiangmei@hebut.edu.cn; slwu@pku.edu.cn

Y. Zhu, Y. Xiang, C. Mao, W. Qiao, J. Wu, J. A. Kubi, K. W. K. Yeung
Shenzhen Key Laboratory for Innovative Technology in Orthopaedic Trauma
Department of Orthopaedics and Traumatology
The University of Hong Kong-Shenzhen Hospital
Shenzhen 518053, China

C. Wang, X. Liu
School of Health Science and Biomedical Engineering
Hebei University of Technology
Tianjin 300401, China

The ORCID identification number(s) for the author(s) of this article can be found under https://doi.org/10.1002/adfm.202406095

DOI: 10.1002/adfm.202406095

exacerbation can result in the formation of fibrous capsules, bone resorption, enzymatic degradation of implants, and ultimately, delayed bone-to-implant integration and eventual implant failure.[2] In fact, implant loosening constitutes more than 10% replacement failures over decades.[7] Therefore, it is essential to timely restore the spatiotemporal osteoimmune microenvironment at the interface between bone and implant (space) following the initial inflammation phase (time) to prevent the progression of chronic inflammation and to create a favorable osteoimmune microenvironment for bone-to-implant integration thereafter.[8]

Current intervention strategies, such as topical and systemic application of anti-inflammation drugs (e. g. NSAIDs) and cytokines (e. g. IL-4), cannot achieve timely regulation of in situ immune responses.[5b,9] Consequently, these methods often require pre-injection and may result in compromised outcomes, as they can interfere with the initial inflammatory stage and potentially cause osteoimmune disturbances due to dose-dependent side effects.[10] Surgical local infiltration can facilitate drug/cytokine delivery to targeted areas, but the invasive procedure may induce additional inflammatory responses,[11] and subject patients to increased pain and distress. In addition to interventional treatments, various strategies have been developed to modify implant surfaces intended to modulate the osteoimmune microenvironment at the bone-to-implant interface. Such modifications include loading biochemical cues such as ions,[12] bioactive polymers,[13] and drugs,[14] or immobilization of biological cues, such as peptides,[15] cytokines,[16] components of cells,[17] bacteria,[18] and fungi.[19] Additionally, local physical stimulations induced by surface topographies have also been explored.[20] Nevertheless, these strategies are limited to the scope of passively regulating immune responses. It remains a great challenge to identify a precise, controllable and non-invasive way to modulate the spatiotemporal osteoimmune microenvironment during specific stages of bone-to-implant integration.

Recently, remote external stimuli have been employed to manipulate cellular behaviors by dynamically the microenvironment of cells and enabling personalized treatments for patients.[21] Among them, NIR has been widely used in antibacterial and cancer treatment due to its power to penetrate biological tissues.[22] TiO_2 that intrinsically exists on the surface of Ti surface is considered to be "bioinert" as it exhibits no cytotoxicity to bone cells or bacteria. However, its wide band gap (3.2 eV) and rapid electron-hole recombination restrict its use in NIR-responsive applications.[23] One strategy to address this issue is creating oxygen vacancies in TiO_2 (TiO_2-V_o) through defective engineering approaches, such as annealing with reductive agents (e.g., Mg and $NaBH_4$ powders) and high-temperature hydrogenation treatment.[24] However, the transition from the bench to the clinic remains challenging due to the complexity of modification methods and biosafety concerns related to the introduction of unstable components.

In this study, we developed an excitable surface capable of proactively and remotely directing the spatiotemporal osteoimmune microenvironment through non-invasive exposure to NIR irradiation. Hydroxyapatite (HA), a desirable, affordable, and biocompatible orthopedic biomaterial,[25] was used as the raw material to prepare the excitable surface via a straightforward laser cladding treatment on titanium (Ti) surfaces. The high-temperature laser cladding process led to the decomposition of hydroxyapatite and reaction with the titanium substrate.[26] Consequently, a defective engineered n–n heterojunction between $CaTiO_3$ and TiO_2-V_o ($CaTiO_3$-TiO_2-V_o) was formed on the excitable surface. The resulted $CaTiO_3$-TiO_2-V_o n-n heterojunction can facilitate the separation of photoinduced charge carriers by a built-in electric field. When exposed to NIR irradiation, the excitable surface generated photoelectric signals that could timely alleviate acute inflammation on demand and establish a favorable osteoimmune microenvironment through spatiotemporal macrophage phenotype switching. The modulated macrophage cytokine profiles thereby encouraged both the recruitment and osteogenic differentiation of MSCs, ultimately leading to enhanced bone-to-implant integration (**Figure 1a**). The favorable osteoimmune modulation effect was demonstrated by significantly accelerated bone-to-implant integration within 14 days post-operation in vivo. The underlying mechanism of the regulatory role of photocurrent on macrophages (using the RAW264.7 cell line) was investigated through transcriptomic analysis, and the findings were subsequently confirmed in vitro. To the best of our knowledge, this is the first study exploring the regulation of immune cells by in situ generated photocurrent in response to noninvasive external physical stimulation. The findings of this study may play a significant role in advancing the creation of novel biomaterials that can remotely control the local immune microenvironment.

C. Ai
Department of Neonatology
Nanfang Hospital
Southern Medical University
Guangzhou 510515, China
W. Qiao
Dental Materials Science
Applied Oral Sciences
Faculty of Dentistry
The University of Hong Kong
Hong Kong 999077, China
S. Wu
School of Materials Science and Engineering
Peking University
Beijing 100871, China
X. Zhao
Department of Applied Biology and Chemical Technology
The Hong Kong Polytechnic University
Hong Kong 999077, China
B. Li
Medical 3D Printing Center
Orthopedic Institute
Department of Orthopedic Surgery
The First Affiliated Hospital
MOE Key Laboratory of Geriatric Diseases and Immunology
School of Biology and Basic Medical Sciences
Suzhou Medical College
Soochow University
Suzhou 215000, China

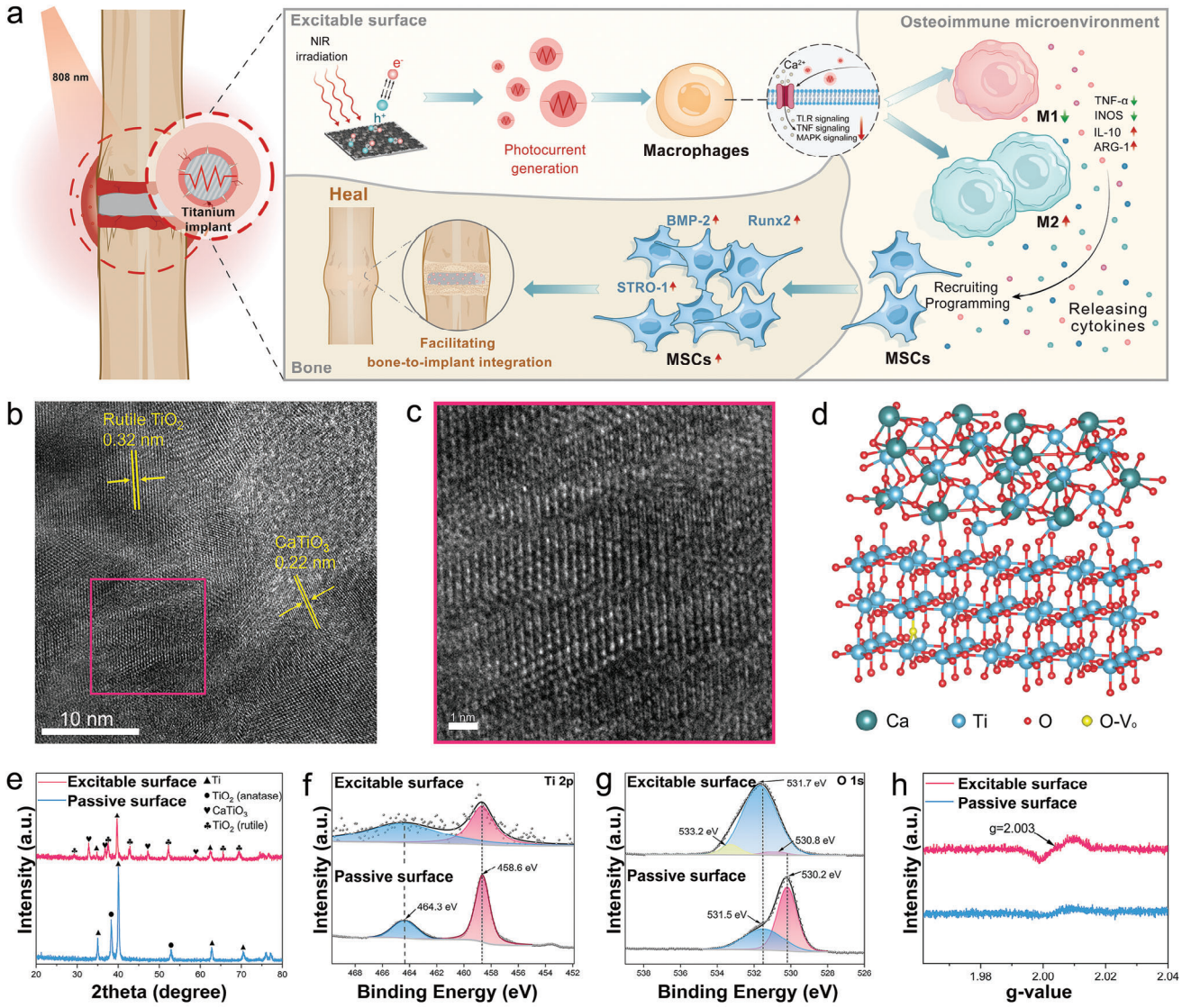

Figure 1. Surface characterization of the excitable surface. a) Scheme illustration showing the design principle of the osteoimmune modulation process to promote osteointegration by the excitable surface. b,c) HR-TEM image of powders scraped from the excitable surface and curved lattice within the red rectangle in the scale bars are 10 and 1 nm, respectively. d) Optimized geometric structures of $CaTiO_3/TiO_2$-V_o heterojunction. e) XRD patterns of the passive surface and excitable surface. f) High-resolution scans for Ti 2p electrons of the passive surface and excitable surface. g) High-resolution scans for O 1s electrons of the passive surface and excitable surface. h) Electron paramagnetic resonance (EPR) spectra of the passive surface and excitable surface.

2. Results and Discussion

2.1. Fabrication and Characterization of the Excitable Surface

The excitable surface was prepared on Ti substrates via laser cladding. Briefly, Ti substrates were first polished before dropping HA dispersion on the surface. After the HA dispersion dried, the samples were treated by laser cladding (Figure S1a, Supporting Information). The surface morphologies of samples were observed using scanning electron microscopy (SEM, Figure S1b,c, Supporting Information). Compared with the polished titanium substrates (passive surface), a rougher surface (Table S1, Supporting Information) with increased hydrophilicity (Figure S1d, Supporting Information) was obtained on the excitable surface. The cross-section image (Figure S1e, Supporting Information) showed that the thickness of the obtained cladding layer was between 100 and 150 µm. To further investigate the excitable surface, scraped powders from the cladding layer were observed using a high-resolution transmission electron microscope (HR-TEM). As shown in Figure 1b, the 0.32 nm lattice spacing of the neighboring lattice fringes corresponded to the (110) crystal plane of rutile TiO_2, whereas the 0.22 nm lattice spacing matched the (022) crystal plane of $CaTiO_3$.[27] In addition, the curved lattice shown in the magnified area (Figure 1c) demonstrated the

existence of lattice defects.[22b] The heteroepitaxial reaction between the $CaTiO_3$ and TiO_2-V_o, as shown in Figure 1d, will be discussed below.

The crystalline structure of the passive surface and the excitable surface were characterized by X-ray diffraction (XRD). As shown in Figure 1e, the passive surface exhibited typical peaks of Ti and anatase TiO_2 peaks, which is ascribed to the spontaneously formed TiO_2 layer on Ti substrate. In comparison, the anatase TiO_2 transformed to rutile TiO_2 on the excitable surface because of the high temperature during the laser cladding process.[26b,28] After the laser cladding treatment, pure HA phase was not found on the excitable surface. Instead, $CaTiO_3$ was found to be the other major component. This was attributed to the decomposition of hydroxyapatite and its reaction with Ti substrate during the high temperature laser cladding process,[26a] the possible reactions between HA and Ti substrates can be represented in equations according to literature:[26b,29]

$$HA + TiO_2 \rightarrow CaTiO_3 + Ca_3(PO_4)_2 + H_2O \quad (1)$$

$$Ca_3(PO_4)_2 + TiO_2 \rightarrow CaTiO_3 + Ca_2P_2O_7 \quad (2)$$

$$Ca_2P_2O_7 + Ti \rightarrow CaTiO_3 + CaO + P_2O_3\uparrow \quad (3)$$

$$P_2O_3 + 3Ti \rightarrow 3TiO_2 + 4P \quad (4)$$

These reactions include the following process: (1) Thermal decomposition of the hydroxyapatite powders under high-temperature laser beams to form $CaTiO_3$ and $Ca_3(PO_4)_2$. (2) Reaction between the decomposition phases of hydroxyapatite ($Ca_3(PO_4)_2$) with TiO_2 on the Ti substrate to form $CaTiO_3$ and $Ca_2P_2O_7$. (3) Thermal decomposition of $Ca_2P_2O_7$ and reaction with Ti to form $CaTiO_3$ with P evaporated in the form of P_2O_3. Therefore, the major component of the excitable surface was TiO_2 and $CaTiO_3$.

X-ray photoelectron spectroscopy (XPS) was used to further investigate the change of surface element states of different samples. The results showed that Ca was incorporated onto the surface of Ti substrates through laser cladding, and the binding energy of Ca corresponded to the chemical state of Ca^{2+} (Figure S2, Supporting Information). Table S2 (Supporting Information) presents the semi-quantitative atomic percentages of the elements. It was observed that the Ti 2p signals from the excitable surface significantly weakened due to the formation of a thick surface structure from the laser cladding process, which obstructed the signals from the Ti substrate. The Ti 2p spectra are shown in Figure 1f, two identical peaks at 458.6 and 464.3 eV were found on the excitable surface, presenting the unchanged chemical state of Ti^{4+} in TiO_2 and $CaTiO_3$.[30] The O 1s spectra are shown in Figure 1g, the characteristic peak of O-metal of the excitable surface exhibited a shift to higher binding energies when compared to that of the passive surface. In addition, a new peak at 533.1 could only be found in the spectra of the excitable surface, which corresponded to O in oxygen-deficient regions.[31] These results indicate that oxygen vacancies were generated on the excitable surface.[24a,31,32] The electron paramagnetic resonance (EPR) was further performed to measure the vacancy in different samples. As shown in Figure 1h, no signal of oxygen deficiency was detected on the passive surface. However, the excitable surface shows an increased EPR signal at a *g*-value of 2.003, which confirms the presence of oxygen deficiencies.[22b,33]

2.2. Photocurrent Generation and Theoretical Calculations

To investigate the photocatalytic activity of the excitable surface under NIR irradiation, the electrochemical impedance (EIS) spectra were first measured (**Figure 2a**). The excitable surface showed lower impedance than the passive surface, indicating the electron transfer resistance was reduced.[34] The excitable surface exhibited lower Photoluminescence (PL) intensity (Figure 2b) than the passive surface, which indicates a lower recombination rate of photoexcited electron-hole pairs.[35] The effective transfer and separation of electron-hole pairs facilitated the photocurrent generation on the excitable surface (Figure 2c). Figure 2d shows the UV–vis–NIR diffuse reflectance (DRS) spectra. The excitable surface showed substantially increased light absorption from 400 to 1200 nm compared with the passive surface. The enhanced absorption could be attributed to the formation of oxygen deficiencies.[36] According to the Tauc-plot (Figure S3, Supporting Information), the bandgap of the passive surface was 3.35 eV, which was attributed to the spontaneously formed TiO_2 layer. In comparison, the calculated bandgap of the excitable surface was narrowed down to 1.69 eV (Figure 2e). However, the energy is still higher than that of 808 nm NIR photons (1.53 eV),[37] which hinders the generation of electron-hole pairs following electron transition under 808 nm NIR irradiation.

To further understand the mechanism of the enhanced generation of NIR light induced photocurrent on the excitable surface, hybrid density functional theory (DFT) calculations were applied. According to the XRD and TEM results, the exposed (110) crystal plane of TiO_2 and the (022) crystal plane of $CaTiO_3$ were selected to simulate the transmission of charge carriers on the excitable surface (Figure 1d). The structure of TiO_2, $CaTiO_3$, and TiO_2-V_o were optimized using first-principal theory (Figure S4, Supporting Information). The total density state (TDOS) of the $CaTiO_3$-TiO_2-V_o heterojunction of the excitable surface were shown in Figure 2f. It is note worthing a new defect level was observed, which could be ascribed to the induction of oxygen vacancies.[38] The location of the defect level was below the aligned Fermi level.[39] The presence of this defect level can promote the separation of photogenerated charge carriers and narrow the band gap with strengthened light absorption,[39] which is consistent with the PL results and DRS analysis. As shown in Figure 2g, the calculated work function of $CaTiO_3$, TiO_2-V_o, and the excitable surface were 3.60, 3.03, and 3.30 eV, respectively. As illustrated in Figure 2h, the valence band (VB) and conduction band (CB) edge potentials of $CaTiO_3$ were −5.82 and −2.42 eV (vs vacuum), respectively. The VB and CB of TiO_2-V_o were −5.96 and −3.26 eV (vs vacuum), respectively. Work functions are commonly used for band alignment in heterostructures.[40] After forming the $CaTiO_3$-TiO_2-V_o contact, electrons in TiO_2-V_o with a lower work function flowed into $CaTiO_3$ with a higher work function.[41] At the interface, the $CaTiO_3$ will accumulate negative charges while the TiO_2-V_o will gather positive charges until two Fermi levels reach an equilibrium level. And this spontaneous interfacial charge transfer leads to the formation of an internal

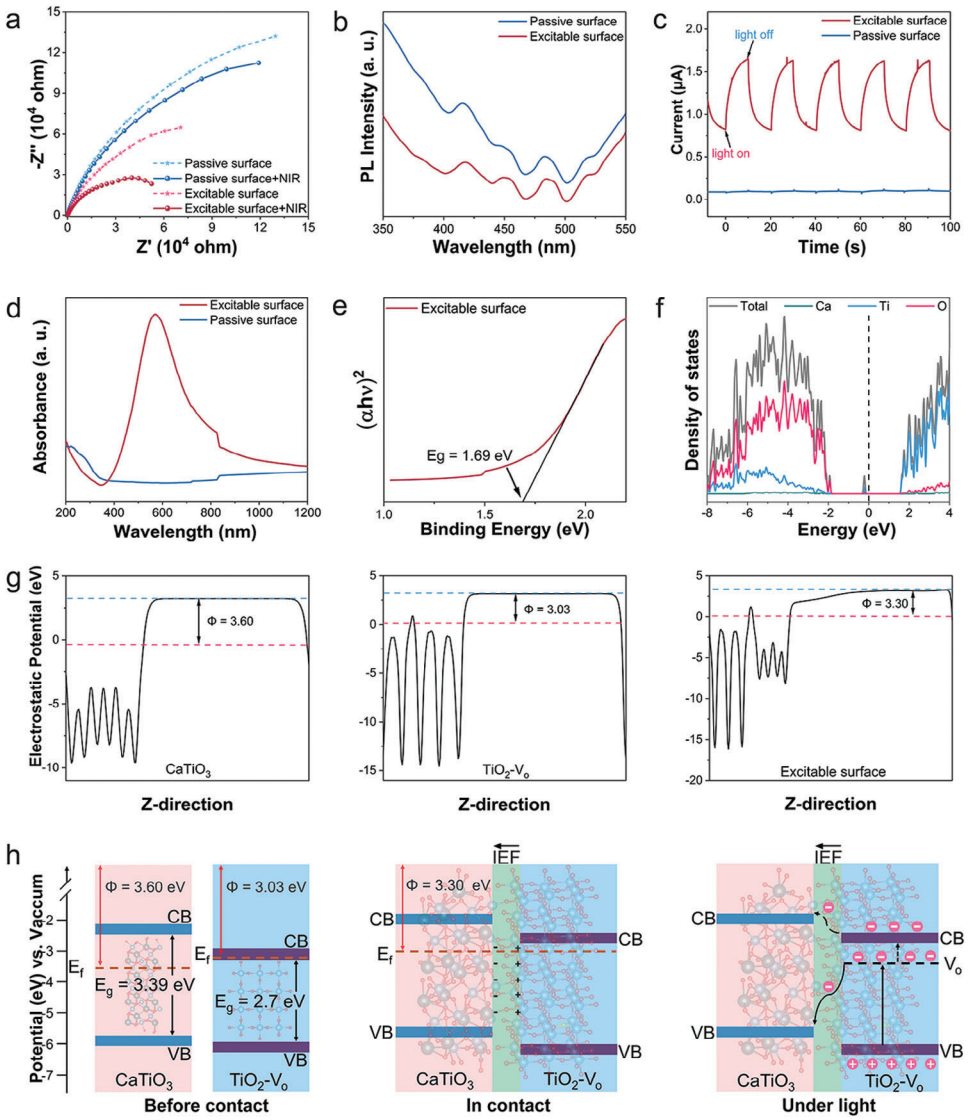

Figure 2. The photoelectric properties of the passive surface and excitable surface. a) EIS tests with or without 808 nm irradiation. b) PL spectra. c) Photocurrent generation under NIR irradiation. d) UV–vis–NIR diffuse reflectance spectra. e) The corresponding taut plots of the excitable surface. f) Calculated TDOS of $CaTiO_3$-TiO_2-V_o heterojunction of the excitable surface. The Fermi energy level is indicated by the vertical dashed line. g) Calculated electrostatic potentials of $CaTiO_3$, TiO_2-V_o, and $CaTiO_3$-TiO_2-V_o heterojunction of the excitable surface, respectively. The red horizontal dashed line denotes the Fermi energy level, whereas the blue horizontal dashed line indicates the vacuum energy level. h) Schematic diagram of band alignment of $CaTiO_3$-TiO_2-V_o heterojunction of the excitable surface.

electric field (IEF) directed from TiO_2-V_o to $CaTiO_3$ at the interface (green region). The strong electrostatic interaction in the internal electric field plays a crucial role in promoting charge transfer between $CaTiO_3$ and TiO_2-V_o. Upon exposure to NIR light, the narrowed bandgap and the V_o defect level enhanced light absorption (Figure 2d). The incident photons were absorbed by the $CaTiO_3$ and TiO_2-V_o heterojunction, promoting electrons from the VB of TiO_2-V_o to the defect level. Driven by the internal electric field, these electrons could further transfer to the $CaTiO_3$ side following two different pathways as indicated in the schematic diagram. Taken together, the $CaTiO_3$ and TiO_2-V_o heterojunction enables the enhanced photocurrent generation on the excitable surface.

2.3. Spatiotemporal Osteoimmune Regulation Accelerated Bone-to-Implant Integration

Growing evidences have demonstrated that the osteoimmune niche induced by macrophages is vital to bone-to-implant integration. As mentioned above, the acute inflammatory stage is indispensable but should not be exacerbated to lead to chronic inflammation. Hence, the inflammation resolution process should not simply aim to terminate the inflammatory response. Instead, it should timely suppress excess inflammation and dynamically assist the transition from classically activated macrophages (M1 phenotype) to alternatively activated macrophages (M2 phenotype). Upon contact between body fluids and implant materials,

M1 macrophages are prone to accumulate around the implant and peak with 24–48 h.[5] Therefore, the time point of NIR irradiation intended to modulate macrophage polarization was set at 48 h after implantation. To determine whether the excitable surface could promptly and effectively alleviate acute inflammation on demand, lipopolysaccharide (LPS) was utilized to induce inflammatory responses in macrophages in vitro. After treated with LPS for 48 h, macrophages were cultured on different samples and treated with or without NIR light irradiation. NIR irradiation conditions were set to circumvent substantial photothermal effect (Figure S5, Supporting Information). Additionally, an interval-based NIR irradiation pattern was performed, transitioning every 20 s between wells to further minimize potential photothermal effect on cells. Results show that the excitable surface could inhibited the secretion of pro-inflammatory cytokines (TNF-α and iNOS) of LPS induced macrophages when subjected to 30 min of NIR irradiation (Figure S6, Supporting Information).

To measure the osteoimmune modulatory effect of the excitable surface and the outcome of bone-to-implant integration in vivo. Samples were implanted into rat tibia defects (**Figure 3a**). NIR irradiation was applied on the sealed skin above the implanted samples 48 h after the surgery.

To evaluate the initial immune responses induced by different implants, a portion of the rats in both the passive surface and excitable surface groups were sacrificed 48 h post-implantation. NIR irradiation was applied at 48 h post-implantation. 48 h post-NIR irradiation, the remaining rats from all four groups (passive surface, passive surface+NIR, excitable surface, and excitable surface+NIR) were sacrificed. The immune responses were evaluated through immunohistochemical staining (Figure S7, Supporting Information) and cytokine levels (Figure 3b). The enzyme-linked immunosorbent assay (ELISA) results revealed that the immune response was intense at 48 h post-implantation, with high secretion levels of both pro-inflammatory and anti-inflammatory cytokines. Notably, we observed that the excitable surface triggered a higher secretion of TNF-α at 48 h post-implantation, but there was no significant difference in the levels of another pro-inflammatory cytokine (iNOS) and anti-inflammatory cytokines (IL-10 and ARG-1). However, 48 h after NIR irradiation, the excitable surface+NIR group exhibited significantly reduced inflammatory responses, as evidenced by lower secretion levels of both TNF-α and iNOS, but higher secretion levels of IL-10 and ARG-1.

Immunohistochemistry staining was then employed to investigate the regulation of macrophages by the excitable surface induced photocurrent under NIR irradiation (Figure S8, Supporting Information). As the general marker CD68 indicated, macrophages were found in all groups, indicating immune cells were infiltrated to the implant area, but no substantial difference was found in different groups. However, semi-quantified results (Figure 3c) show that there was a larger fraction of $CD163^+$ M2 macrophages in the excitable surface+NIR group 14 days after implantation, whereas the fraction of $iNOS^+$ M1 macrophages was lower than other groups. Interestingly, despite the NIR irradiation was only applied for 30 min at 48 h post-surgery, $CD163^+$ M2 macrophages remained dominant in the excitable surface group after 28 days (Figure 3d). These results show that the excitable surface could alleviate the initial acute inflammation stage and promote M2 macrophage polarization under a short period of NIR light irradiation. This spatiotemporal M1/M2 ratio variation may contribute to inducing a favorable osteoimmune microenvironment for bone-to-implant integration.[51] To verify this, we next conducted immunohistochemistry staining to visualize MSCs in the harvested tissue (Figure S9, Supporting Information). Semi-quantified results (Figure 3c,d) show that more $STRO\text{-}1^+$ (surface marker of MSCs) cells were observed in the excitable surface+NIR group at 14 days and lasted for 28 days after implantation, indicating more MSCs were recruited to the implant area. Meanwhile, more runt-related transcription factor 2 (Runx2) and bone morphogenetic protein-2 (BMP-2) positive cells were found in the excitable surface+NIR group. Taken together, these results indicate that the excitable surface+NIR could promote the recruitment and osteogenic differentiation of MSCs.

As shown in Figure 3e,f, the excitable surface+NIR group showed significantly enhanced bone-to-implant integration compared with other groups. Microcomputed tomography (micro-CT) reconstruction was applied to investigate the newly formed bone along the central axis of the implants, with the implant marked in pink and the newly formed bones marked in grey (Figure S10a, Supporting Information). The excitable surface+NIR group presented obviously larger bone volume around the surface of implants at both 14 days and 28 days. Such advantage was further confirmed by the quantification results of bone volume/total tissue volume (BV/TV). In addition, The Safranin-O and Fast Green staining of tibia longitudinally sectioned through the defect site was used to evaluate osteogenic differentiation or cartilage differentiation, with green color representing osteogenic differentiation and red color representing cartilage differentiation (Figure S10b, Supporting Information). At both 14 days and 28 days, higher osteogenic differentiation could be observed around the excitable surface+NIR with an obviously larger green area, which indicated that the excitable surface+NIR could facilitate osteogenesis. Van Gieson's picro-fuchsin staining was employed to further observe the histological conditions around the implants, in which the newly formed bone was stained in red (Figure S10c, Supporting Information). Higher volume and continuous newly formed bone were already visible around the excitable surface+NIR 14 days post operation (Figure 3e). By contrast, only a small amount of new bone appeared around the implants of other groups, including the excitable surface without NIR irradiation. The excitable surface+NIR group also induced substantially more newly formed bone 28 days post-operation. These results demonstrated that the excitable surface+NIR could achieve fast bone-to-implant integration at as early as 14 days post-operation.

2.4. Mechanism of Photoelectrical Instruction on Macrophage Polarization

To understand the underlying mechanism of the regulatory role of photocurrent on macrophage polarization, transcriptomic analysis of RAW264.7 cells cultured on different surfaces with and without NIR irradiation for 48 h was performed. As shown in **Figure 4a**, principal component analysis (PCA) reveals separated clusters of the excitable surface+NIR group with other groups,

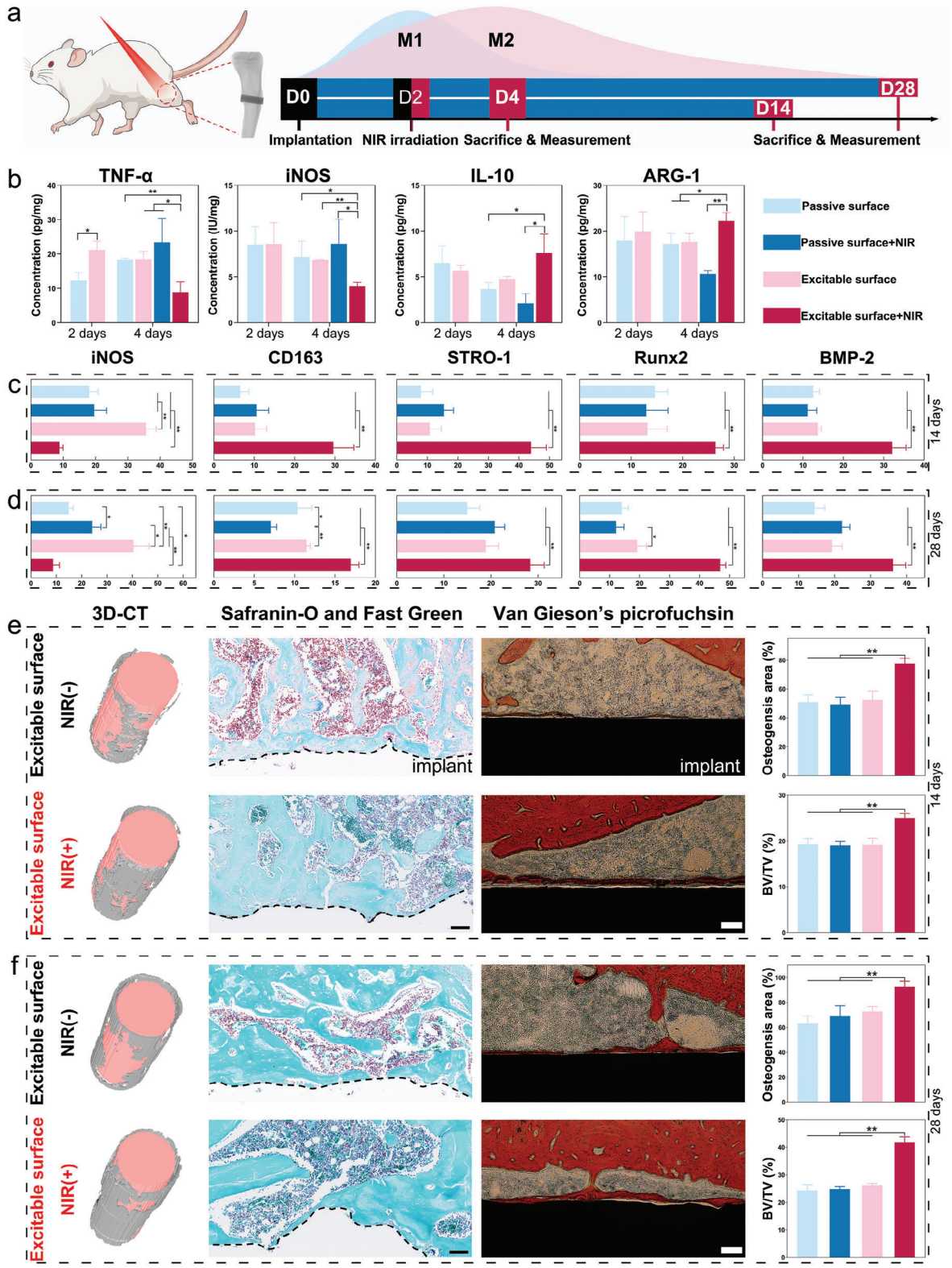

Figure 3. In vivo bone-to-implant integration of the passive surface and excitable surface. a) Schematic diagram of the in vivo study. b) Cytokine secretion level of TNF-α, iNOS, IL-10, and ARG-1, at 48 h post-implantation and at 48 h post-NIR irradiation. c,d) Semiquantification of positively stained cells in the immunohistochemical images of iNOS, CD163, STRO-1, Runx2, and BMP-2 at 14 days and 28 days after implantation. d,e) 3D reconstructed micro-CT, Safranin-O, and Fast Green staining (the scale bar is 100 μm), and Van Gieson's picrofuchsin staining (the scale bar is 200 μm) at 14 and 28 days. n = 3 independent experiments per group, $^{*}p < 0.05$, $^{**}p < 0.01$.

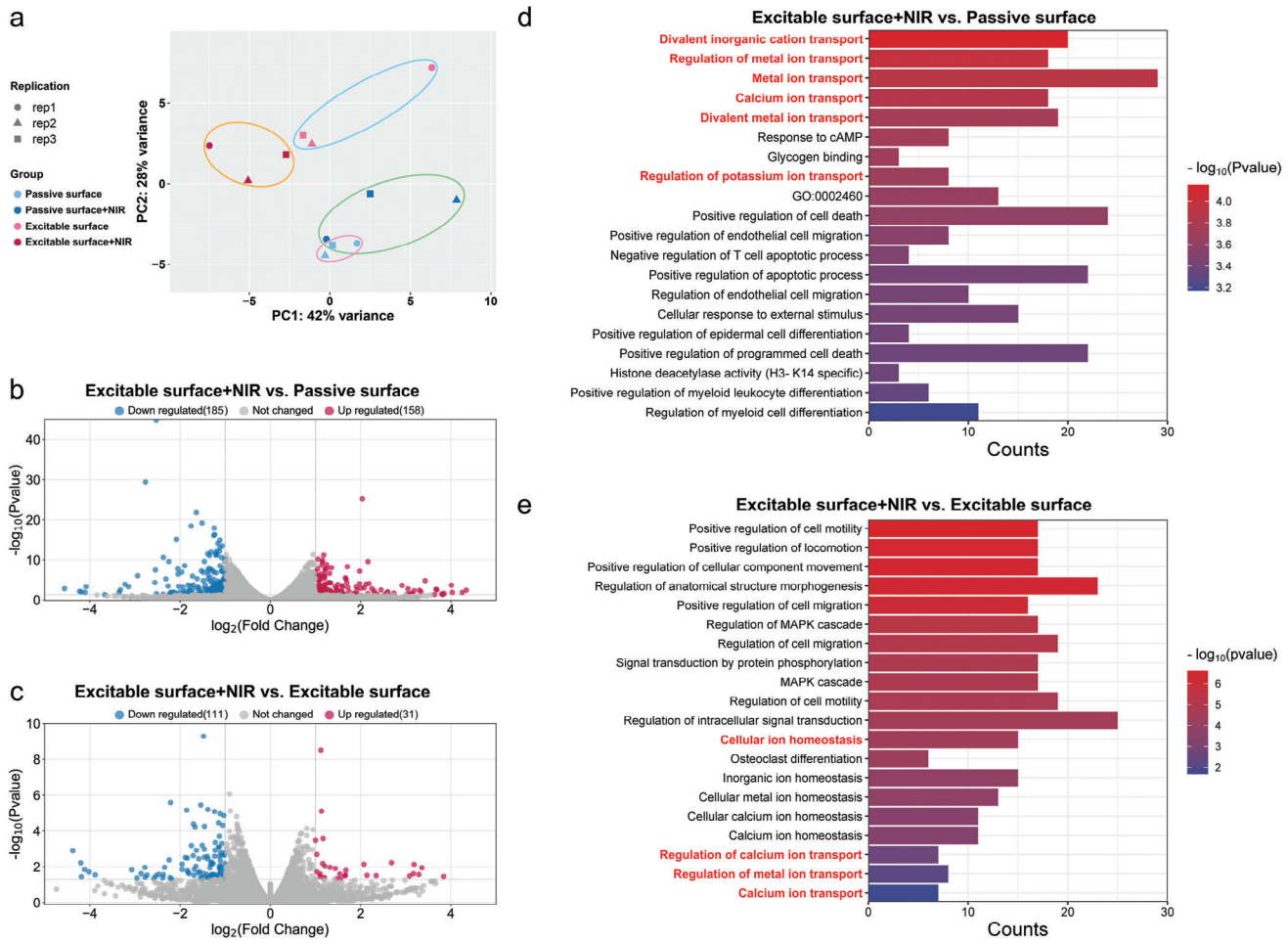

Figure 4. Significantly altered global transcriptome of macrophages on the NIR irradiated excitable surface after 48 h of culturing. a) PCA plot. b,c) Volcano plots displaying gene expression profiles of excitable surface+NIR versus passive surface and excitable surface+NIR versus excitable surface, respectively. d,e) Go analysis of genes of macrophages on the excitable surface+NIR versus the passive surface and the excitable surface+NIR versus the excitable surface, respectively.

indicating distinct transcriptome profiles. This result demonstrated that the NIR induced photocurrent on the excitable surface influenced gene expressions of macrophages. Specifically, volcano plots show there were 185 genes up-regulated genes and 158 down-regulated genes in the excitable surface+NIR compared with the passive surface (Figure 4b). 111 down-regulated genes and 31 up-regulated genes were found in the excitable surface+NIR in comparison to the excitable surface (Figure 4c). At the RNA level, the differentially expressed genes in passive surface versus excitable surface+NIR, and excitable surface versus excitable surface+NIR were collected to perform gene ontology (GO) database analysis (Figure 4d,e). Many of the enriched GO terms were related to voltage-gated ion channels and ion homeostasis, such as regulation of metal ion transport, calcium ion transport and cellular ion hemostasis. Therefore, the regulation of voltage-gated ion channels may play an important role in the photo-electric instructed regulation of macrophages on the excitable surface.

Then, the Kyoto Encyclopedia of Genes and Genomes (KEGG) analysis was performed to investigate the underlying signaling pathways. The KEGG pathways of the excitable surface+NIR versus passive surface and excitable surface+NIR versus excitable surface are shown in **Figure** 5a. Enriched signaling pathways including Toll-like receptor pathways, TNF pathways, and MAPK pathways, were downregulated, as evidenced by the downregulation of mitogen-activated protein kinase kinase kinase 8 (MAP3K8, also known as TPL2) (Figures S11–S13, Supporting Information).[42] These pathways have been reported to be strongly associated with the pro-inflammatory response of macrophages.[43] RT-PCR results (Figure 5b) were consistent with the transcriptomic analysis results. The excitable surface+NIR down-regulated the expression of M1-related gene (TNF-α) but up-regulated the expression of M2-related gene (IL-10). The regulatory role of excitable surface+NIR on macrophage polarization was further confirmed by the secretion level of cytokines. As shown in Figure 5c, excitable surface+NIR induced the secretion of lower amounts of proinflammatory cytokines (TNF-α and iNOS) but higher amounts of anti-inflammation cytokines (ARG-1 and IL-10). Based on the results of GO and KEGG, heatmaps of the expression associated with voltage-gated

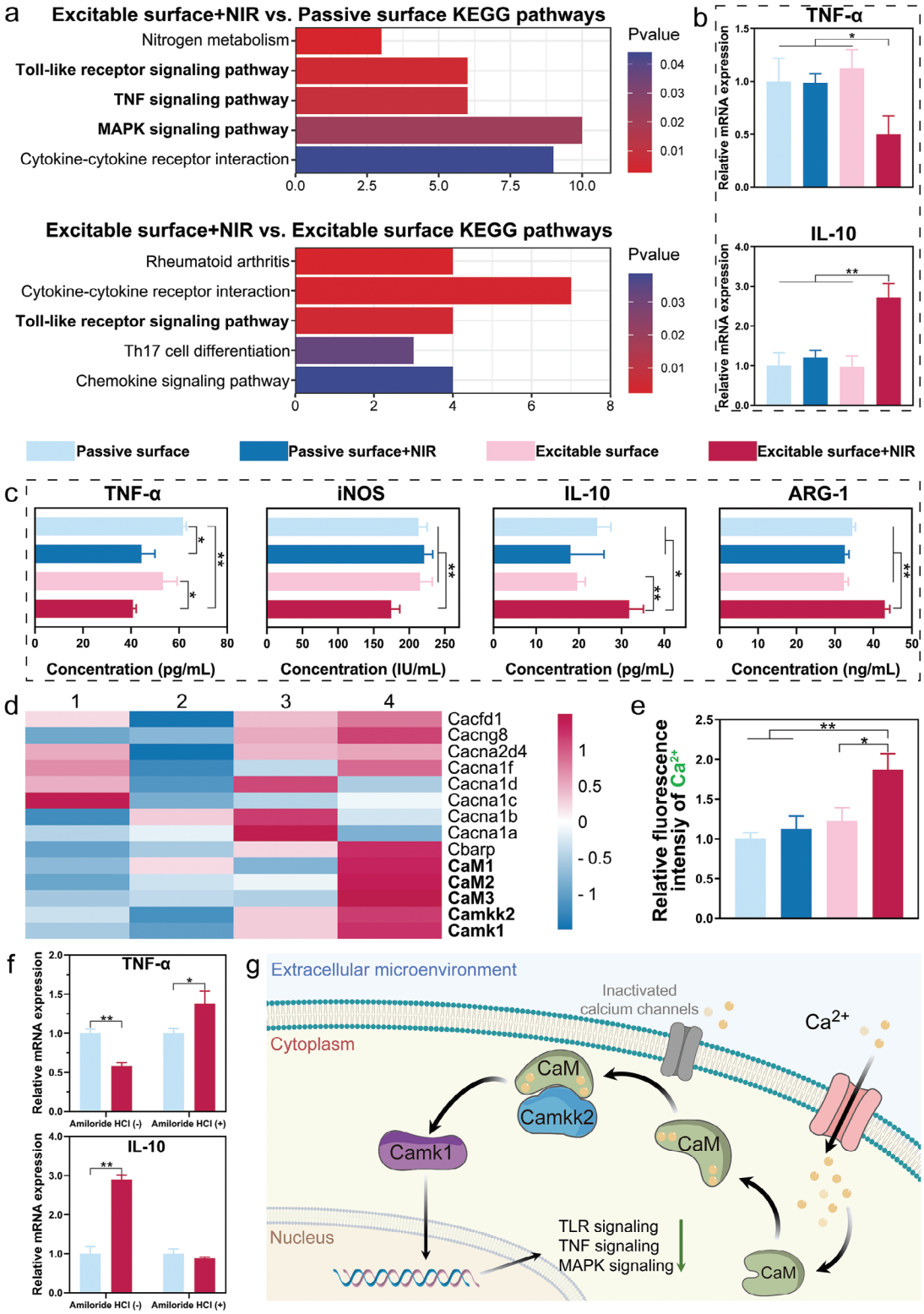

Figure 5. Mechanistic analysis of macrophage polarization regulated by photoelectric signals after 48 h of culturing. a) Enriched KEGG pathways of excitable surface+NIR versus passive surface and excitable surface+NIR versus excitable surface, respectively. b) Relative gene expression level of TNF-α and IL-10. c) ELISA analyses of pro-inflammatory cytokines TNF-α, iNOS, and anti-inflammatory cytokines ARG-1 and IL-10. d) Heatmap analysis of differentially expressed genes related to voltage-gated calcium ion channels (Group: 1. passive surface, 2. passive surface+NIR, 3. excitable surface, 4. excitable surface+NIR). e) Statistical analysis of Ca^{2+} influx fluorescence intensity. f) Relative gene expression level of TNF-α and IL-10 following treatment with amiloride HCl. g) Schematic illustration of the modulation mechanism of photocurrent on macrophages. n ≥ 3 independent experiments per group, $^{*}p < 0.05$, $^{**}p < 0.01$.

ion channels were generated (Figure 5d; Figure S14, Supporting Information). No correlation was found between potassium ion channels, transient receptor potential cation channels, and the regulatory effect of photocurrent on macrophages. In comparison, despite the activation of voltage-dependent calcium channels also varied among different groups, expression levels of calmodulin (CaM), including CaM1, CaM2 and CaM3 were concurrently upregulated in the excitable+NIR group. CaM are ubiquitous intracellular Ca^{2+} receptors,[44] when the Ca^{2+} concentration in the cell increases, they bind to Ca^{2+} and form the CaM/Ca^{2+} complex. Thus, the parallel upregulation of CaM1, CaM2 and CaM3 suggested a positive shift in the balance of calcium channels activation, which facilitated the calcium influx on the excitable surface under NIR irradiation. To confirm whether the photocurrent or the presence of $CaTiO_3$ on the excitable surface could enhance Ca^{2+} influx under NIR light irradiation, Fluo-4 AM staining was utilized to detect Ca^{2+} signals in macrophages following 15 min of NIR irradiation (Figure S15, Supporting Information). Quantification of fluorescence intensity revealed that the excitable surface was unable to promote Ca^{2+} influx in macrophages. However, the Ca^{2+} concentration in macrophages on the excitable surface with NIR irradiation was significantly elevated (Figure 5e). Calcium/Calmodulin-dependent protein kinase kinase 2 (Camkk2) is a central molecular hub involved in multiple cellular functions.[45] Once activated by the accumulated the Ca^{2+}/CaM complex, Camkk2 can further phosphorylates and activates downstream targets like Calcium/calmodulin-dependent protein kinase 1 (Camk1) to influence the inflammation responses.[46] Nonetheless, the impact of Ca^{2+} influx on macrophage polarization remains a contentious topic in the literature. Some studies have reported that calcium influx can induce M1 macrophage polarization,[47] while others have found that Ca^{2+} influx can promote the phosphorylation of CaMKII and facilitate the nuclear localization of Nrf2, ultimately inhibiting M1 macrophage polarization.[48] Shi et al. reported that Ca^{2+} released from CaP coating could promote the transition of M1 macrophages to M2 macrophages by activating the cAMP-PKA pathways.[49] These inconsistencies in the findings could result from differences in physiological conditions, the nature and duration of stimuli, and the extent of Ca^{2+} influx.

Thus, to further investigate the role of Ca^{2+} influx in regulating macrophage polarization, a calcium channel blocker (amiloride HCl) was used to pretreat RAW264.7 macrophages for 1h. After culturing for 48 h, the regulatory role of photocurrent on RAW264.7 macrophages was obliterated. The expression level of TNF-α of the excitable surface+NIR was even higher than that of the passive surface, and no significant difference was found in the expression level of IL-10 (Figure 5f). This further demonstrated that the voltage-gated calcium channels participated in the photocurrent instructed modulation of macrophages. The mechanism is illustrated in the schematic diagram (Figure 5g). When intracellular calcium ion concentration increases, calcium ions bind to the CaM, forming a Ca^{2+}/CaM complex. The Ca^{2+} calmodulin complex activates Camkk2. And then the Activated Camkk2 phosphorylates and activates downstream targets like Camk1 and then downregulated pro-inflammatory pathways including TLR signaling pathway, TNF signaling pathway, and MAPK pathway, which eventually switch the polarization pattern of RAW 264.7 macrophages toward the M2 phenotype.

3. Conclusion

Our results show that the excitable surface could positively direct the local spatiotemporal osteoimmune microenvironment to facilitate bone-to-implant integration via a remotely controlled approach. Upon NIR irradiation, the excitable surface could generate intensified photocurrent. This photo-electrical signal activated the voltage-gated calcium channels to instruct macrophage phenotype switch pattern on the implant surface with M2 macrophages superior in numbers. The cytokine profile includes reduced pro-inflammatory cytokines (TNF-α and iNOS) but increased anti-inflammatory cytokines (ARG-1 and IL-10). This properly instructed favorable osteoimmune microenvironment can significantly accelerate bone-to-implant integration at as early as 14 days post-implantation. The underlying mechanism was primarily investigated through in vitro experiments using the RAW 264.7 cell line. While these cells provide a consistent model, but may not fully emulate the complexity and heterogeneity of primary cells and in vivo models. Additionally, the interaction between the photocurrent and voltage-gated calcium channels in the process needs to be further studied in the future. Despite these limitations, we believe our study presents a novel, controllable, remotely activated, and noninvasive approach to regulating local immune microenvironment. This innovative strategy has the potential to inspire the design of biomaterials and devices capable of precisely modulating local immune microenvironments, thereby improving implant integration and overall clinical outcomes

4. Experimental Section

Preparation of the Excitable Surface: Ti substrates (32 mm diameter and 2.5 mm thick) were obtained from Shunhang Metal Materials Co. (China). HA nanopowder (particle size <100 nm) was purchased from Shanghai Aladdin Biochemical Technology Co., Ltd, (China). The obtained Ti substrates were first polished by sandpaper grinds gradually and then ultrasonically cleaned in ethanol and deionized water for further use. 100 mg of HA nanopowder was dispersed in 10 mL of deionized water by ultrasound dispersion. 800 µL of HA dispersion was dropped on the Ti substrates. The obtained substrates with HA dispersion were dried in an oven at 37°C. Then, laser cladding was performed using a CW 2 kW Nd: YAG laser (Lumonics, JHM-1GY-300B) focused on the substrates. In a typical preparation process, the parameters were set at laser current (I) = 110 A, laser pulse width (W) = 2 ms, laser frequency (f) = 20 Hz, laser spot diameter (D) = 0.6 mm, and scanning speed (V) = 5 mm s^{-1}.

Surface Characterization: The morphology, elemental composition, and phase composition of the obtained excitable surface were investigated by a field-mission scanning electron microscope with energy dispersive X-ray accessory (EDS) (FE-SEM, Zeiss sigma 500, Germany), transmission electron microscope (TEM, JEM-2100F, JEOL, Japan), X-ray photoelectron spectroscopic (XPS, ESCALAB 250Xi, Thermo Scientific, USA) and X-ray diffraction (XRD, D8A25, Bruker, Germany). The surface roughness of samples was measured using an optical profilometer (Contour GT-K 3D, Bruker, Germany). The wettability of samples was measured using a contact angle goniometer (JC2000D2, Powerach, China). The ESR spectra were measured using an EMPplus-10/12 spectrometer (Bruker, German). The UV–vis–NIR absorption spectra were measured using a UV–vis–NIR spectrophotometer (UV-3600, Shimadzu, Japan). The PL spectra were measured using a fluorescence spectro-photometer (Perkin Elmer LS55, USA).

Photo-Responsive Properties of the Excitable Surface: All the photoelectrical measurements were conducted using an electrochemical workstation (CHI660E, Shanghai Chenhua, China). A three-electrode system,

wherein platinum was used as the counter electrode, Ag/AgCl electrode was used as the reference electrode, and Na_2SO_4 (0.5 M) was used as the electrolyte. The EIS spectra and photocurrent generation of different samples were measured under 808 nm NIR irradiation (power density of 0.5 W cm^{-2}).

Theoretical Calculations: All the calculations are performed in the framework of the density functional theory with the projector augmented plane-wave method, as implemented in the Vienna ab initio simulation package.[50] The generalized gradient approximation proposed by Perdew, Burke, and Ernzerhof is selected for the exchange-correlation potential.[51] Heyd–Scuseria–Ernzerhof (HSE) methods are employed for further calculations on band structures. Parameters for the HSE calculations are $\alpha = 0.25$ and $\omega = 0.2$ $Å^{-1}$, which refer to the HSE06 functional. The cut-off energy for plane wave is set to 500 eV. The energy criterion is set to 10^{-5} eV in iterative solution of the Kohn–Sham equation. A vacuum layer of 30 Å is added perpendicular to the sheet to avoid artificial interaction between periodic images. The Brillouin zone integration is performed using 2×2×1 and 4×4×4 k-mesh for slab and bulk models. All the structures are relaxed until the residual forces on the atoms have declined to less than 0.05 eV $Å^{-1}$. The VBM difference between defect TiO_2 ($CaTiO_3$) and pure TiO_2 is calculated using Ti-1s core level alignment based on the Lany–Zunger method, as defined in the following equation:[52]

$$\Delta E_v(A/B) = \Delta E_{v,C'}(B) - \Delta E_{v,C}(A) + \Delta E_{C,C'}(A/B) \quad (5)$$

where A stands for pure TiO_2, and B stands for defect TiO_2. $\Delta E_{v,C'}(B)$ is the energy difference between the VBM and core level of B (i.e., $\Delta E_{v,C'}(B) = E_v(B) - E_{C'}(B)$). Similarly, the energy difference for A is obtained from $\Delta E_{v,C}(A) = E_v(A) - E_C(A)$. $\Delta E_{C,C'}(A/B)$ stands for the difference in the core level of the heterojunction between materials A and B.

In Vitro Responses of Macrophage on the Excitable Surface Under NIR Irradiation: RAW264.7 macrophage cell line was used to evaluate the regulatory role of photo-electric signals on macrophages in vitro. Cells were cultured in Dulbecco's modified Eagle's medium (DMEM, HyClone, USA) with 1% penicillin–streptomycin solution (Gibco, USA) and 10% fetal bovine serum (FBS, Gibco, USA) in an atmosphere of 5% CO_2 incubator at 37°C. The passive surfaces and excitable surfaces were sterilized using 75% ethanol for 1 h and then under ultraviolet light for 30 min before use. RAW264.7 macrophages were cultured on samples in 6-well plates for 12 h first. Then, samples were divided into two groups, one group was treated under NIR light irradiation (power density of 0.5 W cm^{-2}). The irradiation was applied on one well for 20 s and then switch to another, the total irradiation time for each sample will be 30 min. All cells were cultured for 48 h. To evaluate the potential of the excitable surface in reducing acute inflammation induced by M1 macrophages, RAW 264.7 macrophages were pre-treated with LPS (100 ng ml^{-1}) (Sigma, USA) for 48 h. To inhibit the voltage-gated calcium channels, 100×10^{-6} M of amiloride HCl (S1811, Selleck, USA) was added to the culture medium 1 h before NIR irradiation.

To measure the intracellular Ca^{2+} influx of RAW 264.7 cells cultured on different samples. The cells were treated with or without 15 min NIR irradiation, after that, intracellular Ca^{2+} was detected using a fluorescence probe (Fluo-4 AM) according to the manufacturer' s instruction. Staining images were captured with a laser scanning confocal microscope (NIKON Eclipse Ti, Japan). The acquired images (n = 5) were processed using Image Pro Plus software to measure the integrated optical density (IOD) and area. The fluorescence intensity was then calculated using the following formula: fluorescence intensity = IOD per area.

Total RNA from cells was isolated with an RNA kit (OMEGA, USA) and then reverse-transcribed to cDNA using PrimeScript RT Master Mix (TaKaRa, Japan) following the manufacturer's instructions. Real-time PCR was performed on a Bio-Rad RT-PCR system (Bio-Rad, USA) for internal reference glyceraldehyde-3-phosphate dehydrogenase (GAPDH), TNF-α, and IL-10. The primers synthesized are as follows: GADPH, AGGTCGGTGTGAACGGATTTG, and TGTAGACCATGTAGTTGAGGTCA; TNF-α, CCCTCACACTCAGATCATCTTCT, and GCTACGACGTGGGCTACAG; IL-10, GCTCTTACTGACTGGCATGAG and CGCAGCTCTAGGAGCATGTG.

To measure the cytokine secretion of macrophages, the supernatants of RAW264.7 cultured on different groups of samples were collected. The secretion of cytokine, including TNF-α, iNOS, ARG-1, and IL-10 was measured by commercial ELISA kits (Boster Bio, China) following the manufacturer's instructions.

In Vivo Animal Model: To evaluate the osteoimmune modulation effect of photo-electric signals on bone-to-implant integration in vivo, a rat tibia defect model was established using Male Sprague–Dawley rats (250–300 g). All animal experiments were approved by the Animal Research Committee of Shenzhen TopBiotech Co., Ltd., Shenzhen, China (Ethics Approval Number: TOP-IACUC-2023-0216). Rod-shaped samples with dimensions of 2 mm in diameter and 6 mm in length were utilized as implants. Rats were randomly divided into four groups: passive surface, passive surface+NIR, excitable surface, and excitable surface+NIR. The rats were first anesthetized with pentobarbital (30 mg kg^{-1}, 1% w/w). Subsequently, defects were created at the tibia plateau area using a 2 mm diameter drill until the bone marrow was exposed. Samples were then inserted into the defects on both legs of the rats. For the passive surface+NIR and excitable surface+NIR groups, two cycles of 15 min NIR irradiation were applied to the implantation areas 48 h post-surgery.

Detection of Inflammatory Cytokines: To evaluate the modulatory role of photocurrent on local immune microenvironment, a portion of the rats (both passive surface and excitable surface) were sacrificed 48 h post-implantation via overdose of pentobarbital to serve as the control group. Another portion of animals (passive surface, passive surface+NIR, excitable surface, and excitable surface+NIR) were sacrificed 48 h later. The tibia of the rats implanted with different samples were harvested (n = 3). The cytokine secretion levels were evaluated using a modified version of the previously reported method.[3,53] Briefly, the bone tissues around the implants, around 1 cm in length, were grounded into mud using a tissue homogenizer (KZ-II, Servicebio, China) for 3 cycles (60 Hz, 180 s per cycle). The mud of bone tissue was then homogenized in pre-cooled RIPA Lysis and Extraction buffer (ThermoFisher Scientific) for 1 h. The buffer solution was centrifuged at a 12000 rpm for 20 min at 4 °C. The supernatant was then collected for protein concentration quantification using a commercial BCA Protein Assay Kit (Biosharp, China). Equal amounts of protein from each sample were subjected to quantitative analysis of TNF-α, iNOS, IL-10, and ARG-1 using ELISA kits (Shanghai Jianglai Industry Co., Ltd., China) following the manufacturer's instructions.

Micro-CT and Histological Analysis: The rest animals were sacrificed via overdose of pentobarbital at 14 days and 28 days after implantation (n = 6 at each time point). At each time point, samples from each group with tibia were collected. A micro-CT system (SkyScan 1176, SkyScan, Belgium) was used to investigate the harvested tibias with implants (n = 3). The scanning parameters were set as follows: 80 kV source voltage, 313 μA source current, and 345 ms exposure time. The resulting scan images were reconstructed using the CTVol program (SkyScan) to obtain 3D images of the gross bone morphology and microarchitecture surrounding the implants. The new bone volume (BV/TV) values were calculated using the Data Viewer and CTan Program (Skyscan).

The harvested samples were randomly divided for different histological analysis (n = 3). The decalcified samples were embedded in paraffin and sectioned at 5 μm thickness using a Leica RM2016 rotary microtome for immunohistochemistry staining, and Safranin-O and Fast Green staining. For immunohistochemistry staining, samples were first treated with antigen retrieval solution for 20 min and blocked for 1 h min with 5% bovine serum albumin. Then, the samples were incubated with primary antibodies against rat CD68, iNOS, CD163, STRO-1, Runx2 and BMP-2 (all antibodies were purchased from Biosynthesis Biotechnology Inc., China) at 1:100 dilution overnight at 4 °C. After thorough rinsing with PBS, samples were treated with horseradish peroxidase-conjugated secondary antibodies and incubated at 4 °C for 50 min. Following another rinse with PBS, 50–100 μL of freshly prepared 3,3′-Diaminobenzidine (DAB) solution was applied to the tissue sections to allow color development. Afterward, the sections were washed with PBS and counterstained with Hematoxylin. Lastly, the slides were sequentially dehydrated with gradient ethanol (70–100%), cleared with xylene, and coverslipped using mounting solution.

Tissue morphologies were scanned by a Pannoramic Digital Slide Scanner (3DHISTECH, Hungary) and analyzed using CaseViewer software (3DHISTECH, Hungary). The obtained images of each group were randomly selected (n = 3) to semi-quantify the positively stained cells in immunohistochemistry staining images and osteogenesis ratio (green representing osteogenesis while red or orange indicating cartilage) in Safranin-O and Fast Green staining images using the Image-Pro Plus software (Media Cybernetics, USA).

For Van Gieson's picrofuchsin staining, hard tissue processing was applied. Briefly, tibias with samples were first fixed in 10% buffered formalin for 72 h and then dehydrated in gradient ethanol (70%, 95% with two changes, 100% with two changes, each one immersed for 2 days). Subsequently, the samples were treated with two stages of infiltrations: absolute methyl methacrylate (MMA I) for 4 days, followed by MMA II (21 g of dibenzoyl peroxide per 1 L of MMA I) for another 4 days. After that, the samples were immersed in MMA III (40 g of dibenzoyl peroxide and 250 mL of dibutyl phthalate per 1 L of MMA I) in a 37 °C oven for more than 7 days to allow the polymerization of MMA. Finally, the embedded samples were cut into sections longitudinally along the implant and ground to a thickness of 50–70 µm using an EXAKT 300CP system, followed by Van Gieson's picrofuchsin staining. The Van Gieson's picrofuchsin staining was imaged by an inverted fluorescence microscope (IX73, Olympus, Japan).

Transcriptomic Analysis: RAW264.7 macrophage cell suspension (2 mL; 1×10^4 cells ml^{-1}) was cultured on samples in six-well plates and then treated differently as mentioned above. The condition of cell culture and NIR irradiation were consistent with the above-mentioned protocols. After culture, macrophages on samples were lysed by trizol reagent (Thermo Fisher Scientific, USA) and stored at −80 °C before sequencing. RNA sequencing was performed using an Illumina HiSeq X10 (Illumina, USA). The value of gene expression was transformed as log 10 [TPM (Transcripts Per Million reads) + 1]. The data analysis and visualization were performed using a free online platform (www.bioinformatics.com.cn).

Statistical Analysis: All experiments were evaluated as mean values ± standard deviation of at least three tests. A one-way analysis of variance (ANOVA) program combined with a student *t*-test was used to evaluate the statistical significance of the variance. Values of $^{*}p < 0.05$ and $^{**}p < 0.01$ were considered statistically significant.

Supporting Information

Supporting Information is available from the Wiley Online Library or from the author.

Acknowledgements

Y.Z., C.W., and C.A. contributed equally to this work. This work is jointly supported by the National Key Research and Development Program of China (no. 2023YFB3810200), General Research Fund of Hong Kong Research Grant Council (nos. 17214516, 17207719, and 1711322), Hong Kong Innovation Technology Fund (no. ITS/256/22), Hong Kong Health and Medical Research Fund (nos. 20190244, 21200592, 22210832, 23220952, and 09201466), Collaborative Research Fund of Hong Kong Research Grant Council (no. C5044-21G and C7003-22Y), National Natural Science Foundation of China (no. 82201124), Shenzhen Science and Technology Innovation Committee Projects (nos. SGDX20220530111405038, JCYJ20210324120009026, and JCYJ20210324120012034), Guangdong Basic and Applied Basic Research Foundation (no. 2023A1515011963), National Natural Science Foundation of China/Research Grants Council Joint Research Scheme (no. N_HKU721/23), the National Science Fund for Distinguished Youth Scholar (no. 51925104), and National Natural Science Foundation of China (no. 52173251).

Conflict of Interest

The authors declare no conflict of interest.

Data Availability Statement

The data that support the findings of this study are available from the corresponding author upon reasonable request.

Keywords

fast osseointegration, implants, osteoimmunomodulation, oxygen vacancies, photocurrent

Received: April 10, 2024
Revised: September 21, 2024
Published online: October 4, 2024

[1] E. Dondossola, P. Friedl, *Nat. Rev. Mater.* **2022**, *7*, 6.
[2] Y. Chen, Z. Luo, W. Meng, K. Liu, Q. Chen, Y. Cai, Z. Ding, C. Huang, Z. Zhou, M. Jiang, L. Zhou, *Small* **2024**, *20*, 2310325.
[3] W. Qiao, K. H. Wong, J. Shen, W. Wang, J. Wu, J. Li, Z. Lin, Z. Chen, J. P. Matinlinna, Y. Zheng, S. Wu, X. Liu, K. P. Lai, Z. Chen, Y. W. Lam, K. M. C. Cheung, K. W. K. Yeung, *Nat. Commun.* **2021**, *12*, 2885.
[4] C. Shi, E. G. Pamer, *Nat. Rev. Immunol.* **2011**, *11*, 762.
[5] a) T. J. Koh, L. A. DiPietro, *Expert Rev. Mol. Med* **2011**, *13*, e23; b) Z. Zheng, Y. Chen, D. Wu, J. Wang, M. Lv, X. Wang, J. Sun, Z. Zhang, *Theranostics* **2018**, *8*, 5482.
[6] X. Han, J. Shen, S. Chen, Z. Cai, Y. Zhu, W. Yi, K. Li, W. Cai, B. Tao, W. Cui, D. Bai, *Biomaterials* **2023**, *295*, 122057.
[7] J. Linden, *Nature* **2012**, *487*, 179.
[8] a) K. Nathan, L. Y. Lu, T. Lin, J. Pajarinen, E. Jämsen, J. F. Huang, M. Romero-Lopez, M. Maruyama, Y. Kohno, Z. Yao, S. B. Goodman, *Bone Joint Res.* **2019**, *8*, 481; b) T. A. Einhorn, L. C. Gerstenfeld, *Nat. Rev. Rheumatol.* **2015**, *11*, 45.
[9] a) M. Furtado, L. Chen, Z. Chen, A. Chen, W. Cui, *Eng. Regen.* **2022**, *3*, 217; b) J. N. Fullerton, D. W. Gilroy, *Nat. Rev. Drug Discovery* **2016**, *15*, 551.
[10] a) C. D. Buckley, D. W. Gilroy, C. N. Serhan, *Immunity* **2014**, *40*, 315; b) C. D. Buckley, D. W. Gilroy, C. N. Serhan, B. Stockinger, P. P. Tak, *Nat. Rev. Immunol.* **2013**, *13*, 59; c) Y.-C. Chen, S. F. Gad, D. Chobisa, Y. Li, Y. Yeo, *J. Controlled Release* **2021**, *330*, 438.
[11] M. Alieva, J. van Rheenen, M. L. Broekman, *Clin. Exp. Metastasis* **2018**, *35*, 319.
[12] C. H. Lee, Y. J. Kim, J. H. Jang, J. W. Park, *Nanotechnology* **2016**, *27*, 085101.
[13] J. Su, Z. Du, L. Xiao, F. Wei, Y. Yang, M. Li, Y. Qiu, J. Liu, J. Chen, Y. Xiao, *Mater. Sci. Eng. C Mater. Biol. Appl.* **2020**, *113*, 110983
[14] Y. Wei, Z. Liu, X. Zhu, L. Jiang, W. Shi, Y. Wang, N. Xu, F. Gang, X. Wang, L. Zhao, J. Lin, X. Sun, *Biomaterials* **2020**, *257*, 120237.
[15] J. Liu, Y. Tang, W. Yang, B. Tao, Y. He, X. Shen, T. Shen, C. Lin, K. Cai, *Biomater. Sci.* **2019**, *7*, 1463.
[16] Q. Li, B. Liang, F. Wang, Z. Wang, *ACS Biomater. Sci. Eng.* **2020**, *6*, 5215.
[17] F. Wei, M. Li, R. Crawford, Y. Zhou, Y. Xiao, *Acta. Biomater.* **2019**, *86*, 480.
[18] L. Tan, J. Fu, F. Feng, X. Liu, Z. Cui, B. Li, Y. Han, Y. Zheng, K. W. K. Yeung, Z. Li, S. Zhu, Y. Liang, X. Feng, X. Wang, S. Wu, *Sci. Adv.* **2020**, *6*, eaba5723.
[19] Y. Shi, L. Wang, Y. Niu, N. Yu, P. Xing, L. Dong, C. Wang, *Adv. Funct. Mater.* **2018**, *28*, 1804483.
[20] a) R. Sridharan, A. R. Cameron, D. J. Kelly, C. J. Kearney, F. J. O'Brien, *Mater. Today* **2015**, *18*, 313; b) Y. Zhu, H. Liang, X. Liu, J. Wu, C. Yang, T. M. Wong, K. Y. Kwan, K. M. Cheung, S. Wu, K. W. Yeung, *Sci. Adv.* **2021**, *7*, eabf6654.

[21] a) Y. Kim, T. M. Koo, R. Thangam, M. S. Kim, W. Y. Jang, N. Kang, S. Min, S. Y. Kim, L. Yang, H. Hong, H. J. Jung, E. K. Koh, K. D. Patel, S. Lee, H. E. Fu, Y. S. Jeon, B. C. Park, S. Y. Kim, S. Park, J. Lee, L. Gu, D. H. Kim, T. H. Kim, K. B. Lee, W. K. Jeong, R. Paulmurugan, Y. K. Kim, H. Kang, *Adv. Mater.* **2022**, *34*, 2110340; b) S. Y. Kim, R. Thangam, N. Kang, H. Hong, C. Kim, S. Lee, S. Son, H. J. Lee, K. R. Tag, S. Min, D. Jeong, J. Hwang, K. Kim, D. Kim, Y. Kim, J. Joo, B. H. Kim, Y. Zhu, S. G. Park, H. C. Song, W. Sun, J. P. Ahn, W. Y. Jang, R. Paulmurugan, H. K. Kim, J. S. Kim, H. Kang, *Adv. Funct. Mater.* **2023**, *33*, 2215166; c) K. Barri, Q. Zhang, I. Swink, Y. Aucie, K. Holmberg, R. Sauber, D. T. Altman, B. C. Cheng, Z. L. Wang, A. H. Alavi, *Adv. Funct. Mater.* **2022**, *32*, 2203533; d) X. Zhao, L.-Y. Wang, C.-Y. Tang, K. Li, Y.-H. Huang, Y.-R. Duan, S.-T. Zhang, K. Ke, B.-H. Su, W. Yang, *Biomaterials* **2023**, *295*, 122055; e) Y. Kim, R. Thangam, J. Yoo, J. Heo, J. Y. Park, N. Kang, S. Lee, J. Yoon, K. R. Mun, M. Kang, S. Min, S. Y. Kim, S. Son, J. Kim, H. Hong, G. Bae, K. Kim, S. Lee, L. Yang, J. Y. Lee, J. Kim, S. Park, D. H. Kim, K. B. Lee, W. Y. Jang, B. H. Kim, R. Paulmurugan, S. W. Cho, H. C. Song, S. J. Kang, et al., *Adv. Mater.* **2022**, *34*, 2205498.

[22] a) C. Mao, W. Zhu, Y. Xiang, Y. Zhu, J. Shen, X. Liu, S. Wu, K. M. C. Cheung, K. W. K. Yeung, *Adv. Sci.* **2021**, *8*, 2002211; b) K. Su, L. Tan, X. Liu, Z. Cui, Y. Zheng, B. Li, Y. Han, Z. Li, S. Zhu, Y. Liang, X. Feng, X. Wang, S. Wu, *ACS Nano* **2020**, *14*, 2077; c) L. Ma, X. Feng, H. Liang, K. Wang, Y. Song, L. Tan, B. Wang, R. Luo, Z. Liao, G. Li, X. Liu, S. Wu, C. Yang, *Mater. Today* **2020**, *36*, 48.

[23] K. Ozawa, M. Emori, S. Yamamoto, R. Yukawa, S. Yamamoto, R. Hobara, K. Fujikawa, H. Sakama, I. Matsuda, *J. Phys. Chem. Lett.* **2014**, *5*, 1953.

[24] a) X. Han, J. Huang, X. Jing, D. Yang, H. Lin, Z. Wang, P. Li, Y. Chen, *ACS Nano* **2018**, *12*, 4545; b) S. Chen, F. Liu, H. Xin, D. Wen, Y. Zhang, B. Li, Y. Han, *Adv. Funct. Mater.* **2024**, *34*, 2311965.

[25] W. Wang, K. W. K. Yeung, *Bioact. Mater.* **2017**, *2*, 224.

[26] a) C. Han, Q. Wang, B. Song, W. Li, Q. Wei, S. Wen, J. Liu, Y. Shi, *J. Mech. Behav. Biomed. Mater.* **2017**, *71*, 85; b) R. R. Behera, A. Hasan, M. R. Sankar, L. M. Pandey, *Surf. Coat. Technol.* **2018**, *352*, 420.

[27] N. Wei, Y. Chen, X. Wang, M. Kan, T. Zhang, Y. Zhao, *Fundam. Res.* **2022**, *3*, 918.

[28] Y.-C. Lim, Z. Zainal, M. Z. Hussein, W.-T. Tan, *Digest J. Nanomater. Biostruct.* **2013**, *8*, 167.

[29] Z. Jing, Q. Cao, H. Jun, *Ceram. Int.* **2021**, *47*, 24641.

[30] D. Boukhvalov, D. Korotin, A. Efremov, E. Z. Kurmaev, C. Borchers, I. S. Zhidkov, D. Gunderov, R. Valiev, N. Gavrilov, S. O. Cholakh, *Phys. Status. Solidi. B.* **2015**, *252*, 748.

[31] J. Pei, J. Meng, S. Wu, Q. Lin, J. Li, X. Wei, G. Han, Z. Zhang, *J. Alloys Compd.* **2019**, *806*, 889.

[32] B. Wang, M. Zhang, X. Cui, Z. Wang, M. Rager, Y. Yang, Z. Zou, Z. L. Wang, Z. Lin, *Angew. Chem., Int. Ed.* **2020**, *59*, 1611.

[33] Y. Yang, L. C. Yin, Y. Gong, P. Niu, J. Q. Wang, L. Gu, X. Chen, G. Liu, L. Wang, H. M. Cheng, *Adv. Mater.* **2018**, *30*, 1704479.

[34] J. Li, J. Wang, G. Zhang, Y. Li, K. Wang, *Appl. Catal. B: Environ.* **2018**, *234*, 167.

[35] B. Bernardo, D. Cheyns, B. Verreet, R. D. Schaller, B. P. Rand, N. C. Giebink, *Nat. Commun.* **2014**, *5*, 3245.

[36] Z. Wang, C. Yang, T. Lin, H. Yin, P. Chen, D. Wan, F. Xu, F. Huang, J. Lin, X. Xie, M. Jiang, *Energy Environ. Sci.* **2013**, *6*, 3007.

[37] Z. Hua, B. Li, L. Li, X. Yin, K. Chen, W. Wang, *J. Phys. Chem. C.* **2017**, *121*, 60.

[38] Y. Zhang, Z. Xu, G. Li, X. Huang, W. Hao, Y. Bi, *Angew. Chem., Int. Ed.* **2019**, *58*, 14229.

[39] Y. Qin, H. Li, J. Lu, Y. Ding, C. Ma, X. Liu, M. Meng, Y. Yan, *Adv. Powder Technol.* **2020**, *31*, 2890.

[40] A. Agresti, A. Pazniak, S. Pescetelli, A. Di Vito, D. Rossi, A. Pecchia, M. Auf der Maur, A. Liedl, R. Larciprete, D. V. Kuznetsov, D. Saranin, A. Di Carlo, *Nat. Mater.* **2019**, *18*, 1228.

[41] Y. Chen, T. Shi, P. Liu, X. Ma, L. Shui, C. Shang, Z. Chen, X. Wang, K. Kempa, G. Zhou, *J. Mater. Chem. A.* **2018**, *6*, 19167.

[42] a) C. D. Dumitru, J. D. Ceci, C. Tsatsanis, D. Kontoyiannis, K. Stamatakis, J.-H. Lin, C. Patriotis, N. A. Jenkins, N. G. Copeland, G. Kollias, P. N. Tsichlis, *Cell* **2000**, *103*, 1071; b) T. Gantke, S. Sriskantharajah, M. Sadowski, S. C. Ley, *Immunol. Rev.* **2012**, *246*, 168; c) P. B. Dodhiawala, N. Khurana, D. Zhang, Y. Cheng, L. Li, Q. Wei, K. Seehra, H. Jiang, P. M. Grierson, A. Wang-Gillam, K-H. Lim, *J. Clin. Invest.* **2020**, *130*, 4771.

[43] a) A. Sica, A. Mantovani, *J Clin. Invest.* **2012**, *122*, 787; b) H. Zhou, A. P. Coveney, M. Wu, J. Huang, S. Blankson, H. Zhao, D. P. O'Leary, Z. Bai, Y. Li, H. P. Redmond, J. H. Wang, J. Wang, *Front. Immunol.* **2018**, *9*, 3082; c) W. Zhou, Z. Zhu, X. Xiao, C. Li, L. Zhang, Y. Dang, G. Ge, G. Ji, M. Zhu, H. Xu, *Biomed. Pharmacother.* **2021**, *143*, 112181; d) H. L. Park, S. M. Lee, J. K. Min, S. J. Moon, I. Kim, K. W. Kang, S. Park, S. Choi, H. N. Jung, D. H. Lee, J. H. Nam, *Sci. Rep.* **2017**, *7*, 40280.

[44] D. Chin, A. R. Means, *Trends Cell Biol.* **2000**, *10*, 322.

[45] K. L. Marcelo, A. R. Means, B. York, *Trends Endocrin. Met.* **2016**, *27*, 706.

[46] S. N. O'Byrne, J. W. Scott, J. R. Pilotte, A. d. S. Santiago, C. G. Langendorf, J. S. Oakhill, B. J. Eduful, R. M. Couñago, C. I. Wells, W. J. Zuercher, T. M. Willson, D. H. Drewry, *Molecules* **2020**, *25*, 325.

[47] a) X. Zhou, W. Yang, J. Li, *J. Biol. Chem.* **2006**, *281*, 31337; b) A. Chauhan, Y. Sun, P. Sukumaran, F. O. Q. Zangbede, C. N. Jondle, A. Sharma, D. L. Evans, P. Chauhan, R. E. Szlabick, M. O. Aaland, L. Birnbaumer, J. Sharma, B. B. Singh, B. B. Mishra, *IScience* **2018**, *8*, 85; c) M. S. Schappe, K. Szteyn, M. E. Stremska, S. K. Mendu, T. K. Downs, P. V. Seegren, M. A. Mahoney, S. Dixit, J. K. Krupa, E. J. Stipes, J. S. Rogers, S. E. Adamson, N. Leitinger, B. N. Desai, *Immunity* **2018**, *48*, 59.

[48] Z. Lv, X. Xu, Z. Sun, Y. X. Yang, H. Guo, J. Li, K. Sun, R. Wu, J. Xu, Q. Jiang, S. Ikegawa, D. Shi, *Cell Death Dis.* **2021**, *12*, 504.

[49] Y. Shi, W. Tao, W. Yang, L. Wang, Z. Qiu, X. Qu, J. Dang, J. He, H. Fan, *J. Nanobiotechnol.* **2024**, *22*, 47.

[50] G. Kresse, D. Joubert, *Phys. Rev. B.* **1999**, *59*, 1758.

[51] J. P. Perdew, K. Burke, M. Ernzerhof, *Phys. Rev. Lett.* **1996**, *77*, 3865.

[52] S. Lany, A. Zunger, *Phys. Rev. B.* **2008**, *78*, 235104.

[53] W. Qiao, D. Pan, Y. Zheng, S. Wu, X. Liu, Z. Chen, M. Wan, S. Feng, K. M. Cheung, K. W. Yeung, X. Cao, *Nat. Commun.* **2022**, *13*, 535.